Article

3,4-Dihydroxyphenylacetaldehyde synthase evolved an ordered structure to deliver oxygen to pyridoxal 5'-phosphate for cuticle assembly in the mosquito *Aedes aegypti*

Check for updates

Jing Chen[1,2,7], Christopher J. Vavricka [3,7] ✉, Shuangshuang Wei[1,2,7], Yasumoto Nakazawa [3], Yuri Matsumoto[3], Huaqing Chen[1,4], Yu Tang[1], Jing Liang[5], Jiukai Chen[1,2], Yaneng Huang[1,2], Keiichi Noguchi [3], Tomohisa Hasunuma [6], Huai Guan[1], Jianyong Li[5], Chenghong Liao [1,2] ✉ & Qian Han [1,2] ✉

3,4-Dihydroxyphenylacetaldehyde synthase (DHPAAS) catalyzes oxygen-dependent conversion of 3,4-dihydroxyphenylalanine (dopa) to 3,4-dihydroxyphenylacetaldehyde (DHPAA), a likely cross-linking agent precursor of the insect cuticle. In the current study, extensive in vivo experiments in *Aedes aegypti* show that DHPAAS is essential for abdominal integrity, egg development and cuticle structure formation. Solid-state ^{13}C nuclear magnetic resonance analysis of the *Ae. aegypti* cuticle molecular structure shows chemical shifts of 115 to 145 ppm, suggesting the presence of catechols derived from DHPAA. The crystal structure of insect DHPAAS was then solved, revealing an active site that is divergent from that of the homologous enzyme dopa decarboxylase. In the DHPAAS crystal structure, stabilization of the flexible 320–350 region accompanies the positioning of the 350–360 loop relatively close to the catalytic Asn192 residue while the conserved active site residue Phe103 adopts an open conformation away from the active center; these distinct features participate in the formation of a specific hydrophobic tunnel which potentially facilitates delivery of oxygen to pyridoxal 5'-phosphate in the conversion of dopa to DHPAA.

Insect L-3,4-dihydroxyphenylalanine decarboxylase (DDC) is a pyridoxal 5'-phosphate (PLP)-dependent aromatic amino acid decarboxylase (AAAD) that catalyzes the decarboxylation of L-3,4-dihydroxyphenylalanine (dopa), 5-hydroxytryptophan, and structurally similar aromatic amino acids[1]. While mammals often possess a single copy of *AAAD*, insect genomes contain multiple copies of *AAAD* and related genes. *Drosophila melanogaster* contains five *AAAD*-related genes, including one typical *DDC*, two tyrosine decarboxylase-related sequences, and two sequences annotated as α-methyldopa (AMD)-resistant (NP_476592 isoform A and NP_724162 isoform B), which were later characterized as 3,4-dihydroxyphenylacetaldehyde synthase (DHPAAS). Accordingly, AAAD function in insects is diverse with roles in neurotransmitter biosynthesis[2,3], immune responses[4,5], cuticle sclerotization[6,7], and egg-tanning[8].

Previous studies suggested that two *Ae. aegypti* homologs of *D. melanogaster* AMD-resistant protein, encoded by *AAEL010734* and *AAEL010735*, play an essential role in the assembly of the mosquito cuticle[9,10]. Although the two *Ae. aegypti* AMD-resistant proteins share

high sequence identity (51%) to *Ae. aegypti* DDC (AeDDC) (XP_001648264.1), both enzymes were found to convert DOPA to 3,4-dihydroxyphenylacetaldehyde (DHPAA), rather than producing dopamine[9]. Therefore, the *Ae. aegypti* AMD-resistant proteins were renamed as DHPAAS. The transcriptional profile of *Ae. aegypti DHPAAS* (*AeDHPAAS*) closely correlates with cuticle development, and the catalytic product of AeDHPAAS is the reactive aryl acetaldehyde DHPAA that is capable of cross-linking proteins and other components of the insect cuticle[9,11]. Recent studies demonstrated that AeDHPAAS affects larval development and adult survival in *Ae. aegypti* via RNA interference (RNAi)-mediated gene knock-down[12].

The specialized function of *D. melanogaster* AMD-resistant proteins remained a mystery until the mosquito homologs were characterized with DHPAAS activity[9]. Early studies reported that the gene encoding AMD-resistant protein in *D. melanogaster*, confers resistance to the toxic DDC inhibitor AMD[1,13]. Furthermore, a mutation in the gene encoding the AMD-resistant protein was also reported to cause structural defects in the cuticle[11,14,15]. Subsequent studies finally showed that both *D. melanogaster* AMD-resistant proteins exhibit DHPAAS activity[9,16].

Solid-state nuclear magnetic resonance (NMR) is an ideal method for determining molecular structures of insect cuticle, as the cuticle is a complex solid material that cannot be analyzed well in solution or as a crystal due to heterogeneous assembly of the component molecules[17–21]. Previous solid-state NMR studies have indicated that catechol-containing structures are present as cross-links in the cuticles of a few insects, especially *Manduca sexta*[17–20]. Accordingly, there seems to be a consensus that the DHPAAS enzymatic product DHPAA is involved in the assembly of un-melanized cuticle; however, the elucidation of DHPAA as a direct precursor of cuticle catechols and the solid-state NMR analysis of mosquito cuticle are both lacking. Therefore, the precise role of DHPAAS in cuticle formation and the catalytic mechanism of DHPAAS need to be clarified. Furthermore, while the crystal structure of *D. melanogaster* DDC (DmDDC) has been reported[22], novel loop structures near the active site of insect DHPAAS cannot be correctly modeled based on the homologous DmDDC structure template; therefore, it is necessary to solve the DHPAAS crystal structure in order to understand the structural basis of its novel reaction.

The current study aims to clarify the precise function of DHPAAS in insect cuticle formation, by characterizing DHPAAS throughout the physiological level down to the molecular level. Physiological investigations confirm that AeDHPAAS is essential for the development of insect cuticle, where *AeDHPAAS* knockdown impairs blood meal intake, abdominal integrity, egg hatching, and cuticle structure at the µm and molecular levels. To view the three-dimensional molecular level, the crystal structure of *D. melanogaster* DHPAAS (DmDHPAAS) in complex with PLP was solved, revealing a more ordered 320–350 region in comparison to that of homologous DmDDC. The relatively ordered 320–350 region appears to influence movement of the Leu353- and Phe103-containing loops towards and away, respectively, from the catalytic Asn192 residue of the neighboring DmDHPAAS subunit, and leads to the opening of a hydrophobic tunnel with potential to deliver oxygen[23] to the substrate binding side of lysine-linked PLP (LLP). DmDHPAAS Phe103 and the corresponding Phe106 residue of AeDHPAAS remain far enough from LLP that the potential oxygen tunnels can continue to access the substrate binding face of LLP throughout molecular dynamics simulations. These distinct structural features of insect DHPAAS provide a structural basis underlying the catalytic production of the essential cuticle intermediate DHPAA.

Results

Abdominal integrity varies between male and female adult mosquitoes
Before selecting adult mosquitoes for *AeDHPAAS* knock-down experiments, male and female adult mosquitoes were initially compared for their ability to handle abdominal injections. The abdomens of both male and female adult mosquitoes were flat before the injection of Ringer's solution, an isotonic salt solution[24] (Supplementary Fig. 1a, d). After injection with Ringer's solution, the abdomens of both male and female adults swelled (Supplementary Fig. 1b, c, e, f). These initial results showed that female adults could survive after injection of 3–5 µL solution, but male adults could only survive after being injected with 0.3–0.4 µL solution at most (Supplementary Fig. 2). Based on the abdominal injection results, female adult mosquitoes were selected for subsequent RNAi experiments.

DHPAAS knock-down increases mortality and reduces blood meal intake
Adult female mosquitoes were collected 12 h after RNAi microinjection to analyze gene expression. Real-time PCR (qPCR) showed no significant difference between *gus*-dsRNA injected and DEPC-injected controls, while the relative expression of *AeDHPAAS* in the RNAi group was significantly lower (75% lower, $P < 0.001$) than that in the control groups (Fig. 1a). Meanwhile, very few female adults in the control groups died after 4 µL of Ringer's solution injection, but approximately 50% ($P < 0.0001$) of the adults with *AeDHPAAS* knock-down failed to survive (Fig. 1b). The weight of adult mosquitoes before and after blood meal was measured, as shown in Fig. 1c, and no significant weight differences were observed between control and experimental groups. The average weight of each female adult was 1.7–1.8 mg (Fig. 1c). Figure 1d illustrates blood meal intake weight, where the blood meal weight of adults in the control groups ranged from 3.7 to 4 mg, while the blood meal weight of adults with *AeDHPAAS* knock-down was only around 2 mg ($P < 0.0001$).

DHPAAS knock-down disrupts the abdominal cuticle
After RNAi knock-down of *AeDHPAAS*, followed by oviposition, $40 \pm 3.3\%$ of the adult female mosquitoes died within 3 days (Supplementary Fig. 3). In contrast, only 5% failed to survive in the DEPC-treated and *gus*-dsRNA treated control groups under matching conditions. Furthermore, $25 \pm 5\%$ of the mosquitoes that survived after *AeDHPAAS* knock-down showed lowered tolerance to the abdominal injection of Ringer's solution, with a relatively high frequency of abdominal rupturing (Fig. 2).

DHPAAS knock-down reduces egg hatching
RNAi knock-down of *AeDHPAAS* had no significant effect on the number of eggs, where each mosquito produced 100 ± 20 eggs (Fig. 3a). However, hatching of eggs was significantly inhibited by *AeDHPAAS* knock-down. The egg hatching rates of the control groups and the *AeDHPAAS*-dsRNA treated group were $90 \pm 5\%$ and $53 \pm 28\%$, respectively (Fig. 3b). Approximately 60% of the non-hatching eggs of the *AeDHPAAS*-dsRNA treated group contained no larvae, but all eggs of the control groups contained developed larvae. These non-hatching eggs without larvae in the *AeDHPAAS*-dsRNA treated group rapidly dehydrated after reducing humidity from 20 to 10%; control group eggs did not dehydrate with decreased humidity (Fig. 3c). The remaining (~40%) non-hatching eggs of the *AeDHPAAS*-dsRNA treated group contained formed larvae and did not dehydrate; however, none of these eggs could hatch.

DHPAAS knock-down alters cuticular structure
During mosquito cuticle formation, the epithelium first secretes cuticulin and then the lamellate endocuticle. Finally, the exocuticle is derived by quinone tanning of the outer lamellae of the endocuticle[25]. To observe the effect of *AeDHPAAS* knock-down on cuticle formation, transmission electron microscopy (TEM) was used to observe abdominal cuticular structures 12 h after microinjection. The resulting TEM images showed that the endocuticle was thicker than the exocuticle in the control groups (Fig. 4a, b). In contrast, the *AeDHPAAS*
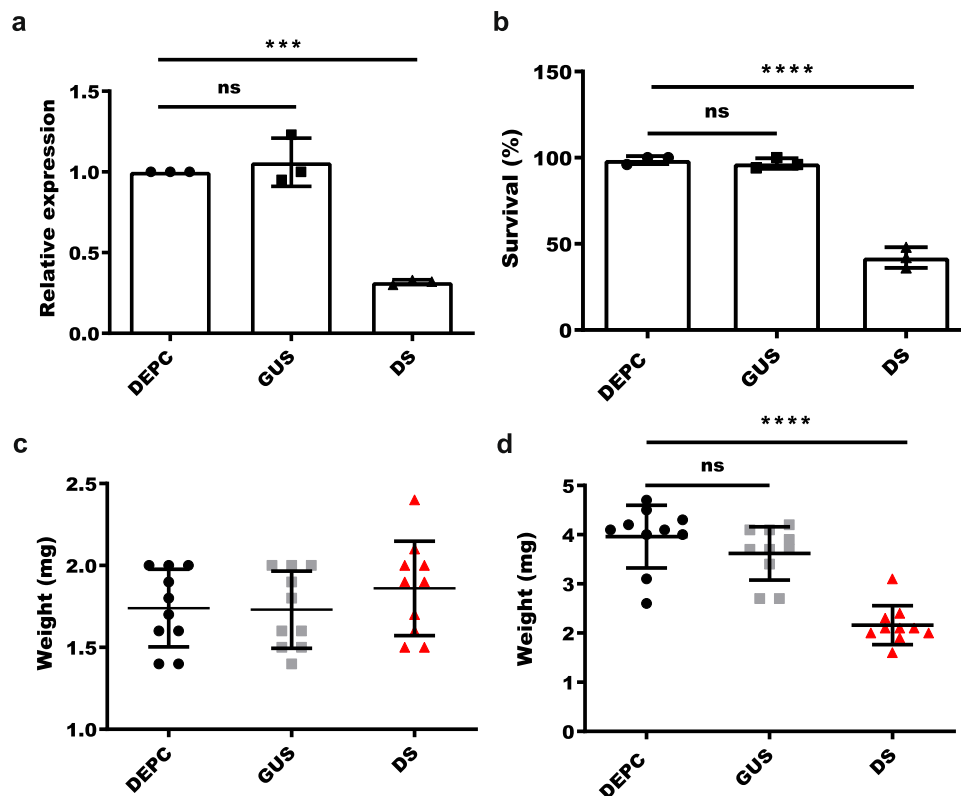
Fig. 1 | Knock-down of *AeDHPAAS* in female adult mosquitoes. a *AeDHPAAS* transcript abundance after RNAi was detected by qPCR. Twelve mosquitoes were analyzed per group, and the experiment was replicated three times. DEPC 95% confidence interval (CI) = 1.00–1.00; GUS 95% CI = 0.93–1.18; DS 95% CI = 0.26–0.33. DEPC vs GUS, $Q = 3.04$, degrees of freedom (df) = 6, $P = 0.14$; DEPC vs DS, $Q = 40.30$, df = 6, $P < 0.001$. **b** Female mosquito survival, 12 h after injection with Ringer's solution following RNAi. 100 mosquitoes were analyzed from each group, and the experiment was replicated three times. DEPC 95% CI = 92.93–104.40; GUS 95% CI = 89.08–104.26; DS 95% CI = 27.09–56.90. DEPC vs GUS, $Q = 0.84$, df = 6, $P = 0.42$; DEPC vs DS, $Q = 23.88$, df = 6, $P < 0.0001$. **c** Mosquito weight after RNAi and before blood meal. 15 mosquitoes were analyzed from each group, and the experiment was replicated ten times. DEPC 95% CI = 1.57–1.91; GUS 95% CI = 1.56–1.90; DS 95% CI = 1.65-2.07. DEPC vs GUS, $Q = 0.12$, df = 27, $P = 0.93$; DEPC vs DS, $Q = 1.49$, df = 27, $P = 0.32$. **d** Blood meal weight after RNAi. 15 mosquitoes were analyzed from each group, and the experiment was replicated 10 times. DEPC 95% CI = 3.50-4.42; GUS 95% CI = 3.23–4.00; DS 95% CI = 1.88–2.67. DEPC vs GUS, $Q = 2.02$, df = 27, $P = 0.21$; DEPC vs DS, $Q = 10.67$, df = 27, $P < 0.0001$. X-axes represent different treatment groups, and y-axes represent relative *AeDHPAAS* expression (**a**), survival rate (**b**), mosquito weight (**c**), and blood meal weight (**d**). Data were presented as mean values ± standard deviation (SD). Ordinary one-way analysis of variance (ANOVA) with two-sided Tukey's multiple comparisons test was used. *** indicates $P < 0.001$; **** indicates $P < 0.0001$; ns indicates no significance. Source data are provided as a Source Data file. DEPC mosquitoes treated with diethylpyrocarbonate (DEPC)-treated water, GUS mosquitoes treated with *gus*-dsRNA, DS mosquitoes treated with *AeDHPAAS*-dsRNA.

RNAi group showed a thinner endocuticle layer relative to the exocuticle (Fig. 4c).

Catechol ring containing compounds are observed in mosquito cuticle

To observe the molecular structure of the cuticle, solid-state ^{13}C NMR analyses were performed. Chemical shifts of 115 to 145 ppm, corresponding to catechol ring carbons, could be observed in the ^{13}C cross-polarization/magic angle spinning (CP/MAS) NMR spectrum[26] of the *Ae. aegypti* cuticle sample (Fig. 5 and Supplementary Figs. 4, 5). In particular, the broad peak observed at 145 ppm can be attributed only to the carbon nuclei at positions 3 and 4 of the catechol ring. This result supports the hypothesis that the catechol ring of DHPAA is present in mosquito cuticle, but the precise catechol structures in the observed spectra should be confirmed in future studies.

Changes in peak intensity corresponding to changes in CP time can provide insight into site-specific dynamics[27–29]. CP contact time-dependent ^{13}C CP/MAS NMR spectra of the cuticle sample (Supplementary Fig. 6) showed interesting differences in CP time-dependent changes in peak intensity for NMR peaks corresponding to the chitin, protein and lipid components, in comparison to the peaks corresponding to the catechol ring. However, CP-transfer rates also vary significantly depending on the functional group of the signal-producing carbon[28,29]. On the other hand, ^{13}C spin-lattice relaxation time (T_1^{C}) measurements (Supplementary Table 1) show relatively long T_1^{C} values for a major component of the catechol ring peaks, suggesting that catechol rings are present in a rigid state[30,31]. Together, the provided solid-state NMR results are consistent with the hypothesis that DHPAA is a cross-linking precursor that may stabilize cuticle structures.

DHPAAS knock-down alters gene expression

Knock-down of *AeDHPAAS* in *Ae. aegypti* larvae (Supplementary Fig. 7) resulted in obvious abnormal exfoliation and delayed larval development. To further explore the functional role of *AeDHPAAS* in larval development and molting, gene expressions of *AeDHPAAS* RNAi and control groups were focally analyzed using RNA-seq. Genes that were significantly differentially expressed between the experimental group and both *gus*-dsRNA-injected and DEPC-injected control groups could then be analyzed. The differentially expressed genes involved in development were analyzed according to predefined pathways annotated by the Kyoto Encyclopedia of Genes and Genomes (KEGG)[32–34]. As a result, 59 development-related genes were found to be differentially expressed after *AeDHPAAS* knock-down, of which only five genes were upregulated while the rest were downregulated (Fig. 6a).
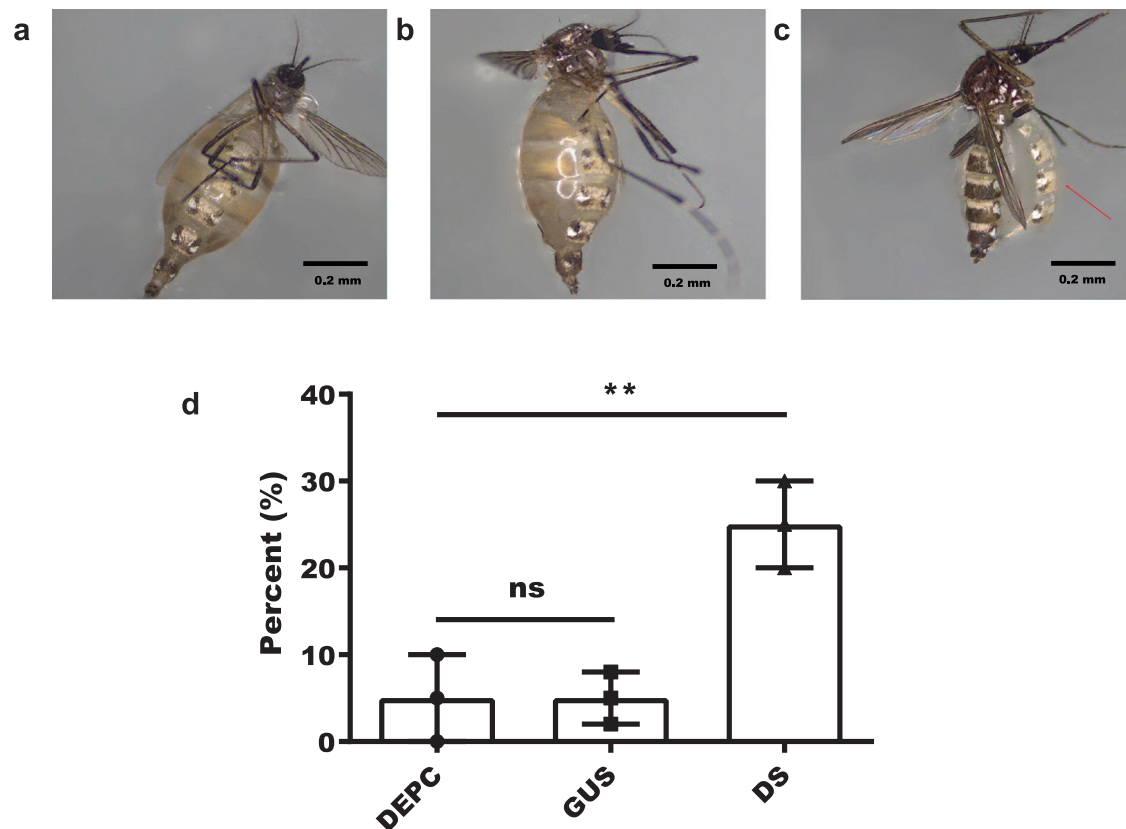
Fig. 2 | Abdominal condition of adult female mosquitoes injected with Ringer's solution. a–c Treated mosquitoes that survive 72 h after laying eggs were then injected with 5 μL Ringer's solution. **a** Surviving mosquito first treated with DEPC water, and then injected with Ringer's solution. **b** Surviving mosquito treated with *gus*-dsRNA, and then injected with Ringer's solution. **c** Surviving mosquito treated with *AeDHPAAS*-dsRNA, and then injected with Ringer's solution. **d** The percentage of mosquitoes from each group with abdominal rupturing. Thirty female adults were analyzed from each group, and the experiment was replicated three times. Data were presented as mean values ± SD. Ordinary one-way ANOVA with two-sided Tukey's multiple comparisons test was used for statistical analysis. DEPC 95% CI = -7.42–17.42; GUS 95% CI = -2.45–12.45; DS 95% CI = 12.58–37.42. DEPC vs GUS, $Q = 0.00$, df = 6, $P > 0.99$; DEPC vs DS, $Q = 7.81$, df = 6, $P < 0.01$. ** indicates $P < 0.01$; ns indicates no significant difference. Source data are provided as a Source Data file. DEPC mosquitoes treated with DEPC water, GUS mosquitoes treated with *gus*-dsRNA, DS mosquitoes treated with *AeDHPAAS*-dsRNA.

Our previous research has shown that knock-down of *AeDHPAAS* can cause abnormal larval molting[12], and our current solid-state NMR results show chitin, protein, and lipid as major components of the *Ae. aegypti* cuticle. Accordingly, the expression of genes related to cuticle proteins, chitin metabolism, and lipid metabolism were altered after knock-down of *AeDHPAAS*. Compared with the control groups, 117, 106, and 109 genes related to cuticle proteins, chitin metabolism, and lipid metabolism, respectively, were differentially expressed (NCBI BioProject database, accession PRJNA1130691) (Fig. 6b–d). Most of these differentially expressed genes showed trends of upregulated expression. Nine out of 117 differentially expressed cuticle genes related to cuticle proteins were downregulated (Fig. 6b), 24 out of 106 genes involved in chitin metabolism were downregulated (Fig. 6c), and 27 out of 109 genes involved in lipid metabolism were downregulated (Fig. 6d). In addition, interesting changes in the expression of sterol carrier protein 2 (*SCP-2*) and lipophorin receptor (*LpR*) genes were observed in *Ae. aegypti*. Five out of eight *SCP-2* genes were significantly upregulated, and a single *LpR* gene was significantly down-regulated (Fig. 6e).

The crystal structure of insect DHPAAS reveals distinct features
After purification and crystallization of DmDHPAAS, the crystal structure of DmDHPAAS was solved using molecular replacement based on the DmDDC structure (PDB ID 3K40)[22]. The crystal structure was refined to 2.2 Å resolution with crystallographic statistics shown in Supplementary Table 2, and the structure was deposited and released

(PDB ID 6JRL). According to analysis of the protein interfaces, surfaces, and assemblies service[35], the DmDHPAAS crystal structure is a dimer (Supplementary Fig. 8). The overall DmDHPAAS structural architecture resembles other type II PLP-containing enzyme structures.

The DmDHPAAS active site is located at the monomer-monomer interface of the homodimer and is mainly composed of residues from a single subunit; however, the Phe103- and Leu353-containing loops support the formation of the active site of the neighboring subunit. The active site Lys303 is observed to form a Schiff base with the PLP cofactor, and this internal aldimine is referred to as LLP (Fig. 7).

Like most PLP-dependent enzymes, the LLP protonated pyridine nitrogen forms a salt bridge with the Asp271 carboxylate[36]. Furthermore, the LLP pyridine ring is anchored by the Ala273 methyl group as well as the catalytic Asn192 amide group. The LLP pyridine ring hydroxy group is adjacent to the Thr246 side chain and two water molecules. The LLP phosphate moiety is further stabilized by multiple interactions with Ser149, Asn300, and His302 from within the same subunit, and is 5.0 Å from Leu353 of the neighboring subunit (Fig. 7a).

In the DmDHPAAS structure, the loop containing Phe103 is much further away from LLP and the catalytic 192 residue in the active site center, in comparison to the active site of the closest related enzyme DmDDC (Fig. 7b, c). Here, Asn192 and His192 are critical for determining DmDHPAAS and DmDDC catalytic activity, respectively (Fig. 7g)[9,37].

The DmDHPAAS region spanning residues 320–350 forms more defined structures as compared to that of DmDDC (Fig. 7b). The
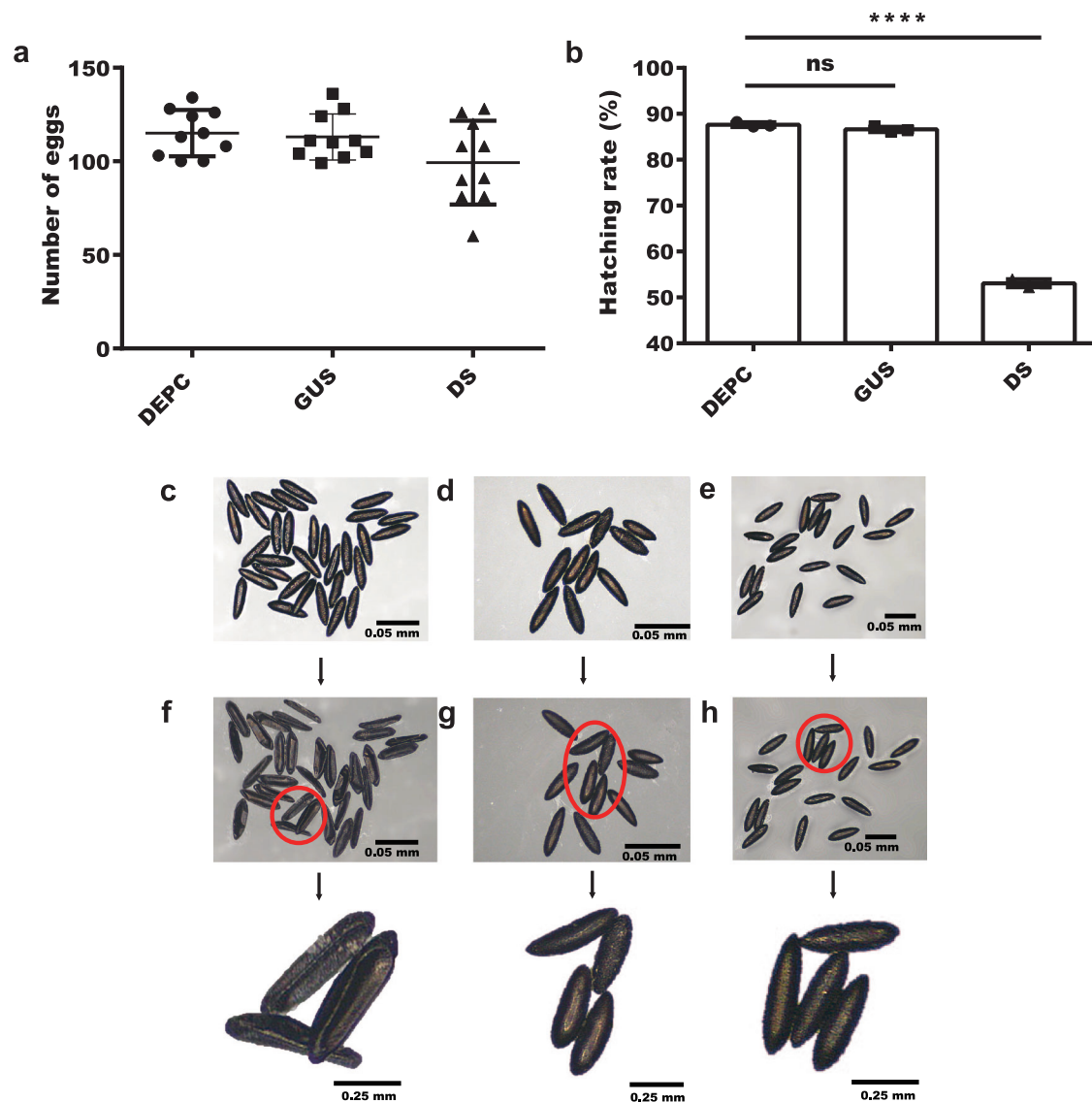
Fig. 3 | *AeDHPAAS* impacts egg hatching. a Number of eggs per mosquito. The x-axis represents the number of eggs from adult mosquitoes in each group. Fifteen female adults were analyzed from each group, and the experiment was replicated ten times. Ordinary one-way ANOVA was used for statistical analysis. DEPC 95% CI = 106.25-123.96; GUS 95% CI = 104.23-121.77; DS 95% CI = 83.33-115.27. DEPC vs GUS, Q = 0.41, df = 27, P = 0.71; DEPC vs DS, Q = 3.06, df = 27, P = 0.07. **b** Egg hatching rate. The x-axis represents DEPC, GUS, and DS groups. 50 independent samples were analyzed from each group, and the experiment was replicated three times. DEPC 95% CI = 86.33-88.95; GUS 95% CI = 85.15-88.07; DS 95% CI = 50.92-55.24. DEPC vs GUS, Q = 2.36, df = 6, P = 0.23; DEPC vs DS, Q = 88.16, df = 6, P < 0.0001. Data were presented as mean values ± SD. An ordinary one-way ANOVA with two-sided Tukey's multiple comparisons test was used for statistical analysis. **** indicates P < 0.0001; ns indicates no significant difference. Source data are provided as a Source Data file. **c**–**e** Images of eggs stored under 20% humidity. **f**–**h**, Images of corresponding eggs after humidity was reduced to 10%. **c** and **f** show eggs from the DS group; **d** and **g** show eggs from the DEPC group; **e** and **h** show eggs from the GUS group. DEPC mosquitoes treated with DEPC water, GUS mosquitoes treated with *gus*-dsRNA, DS mosquitoes treated with *AeDHPAAS*-dsRNA.

disordered region of DmDHPAAS only includes residues 328–341 (14 residues of Fig. 7f) whereas the disordered region of DmDDC includes residues 322–348 (27 residues of Fig. 7f). The relatively stabilized 323–327 and 342–351 regions of DmDHPAAS are observed to influence the Leu353-containing loop adjacent to the active site; DmDHPAAS Leu353 residue is positioned just 3.4 Å away from the catalytic Asn192 residue, whereas the corresponding Leu350 residue in DmDDC is oriented much further away from the active site (Fig. 7b). In this DmDHPAAS active site conformation, Trp71, Tyr79, Tyr80 and Asn192 from one subunit, and Ile101, Phe103, Leu353 and Gly354 (important for dopa specificity[38]) from the neighboring subunit form the end of a hydrophobic tunnel leading to the substrate binding side of LLP (Fig. 7d). This DmDHPAAS hydrophobic tunnel leads to both LLP molecules across each subunit, contains an additional branch opening up to the surface of the protein near Ser193 in both subunits, and does not exist in the DmDDC crystal structure (Fig. 7e).

AeDHPAAS and DmDHPAAS show similar molecular dynamics

To construct a valid full-length AeDHPAAS model, the crystal structure of DmDHPAAS (PDB ID 6JRL, chain A) was selected as the most satisfactory template, with sufficient homology to AeDHPAAS (61% identify and 92% coverage). The MODELLER program was used to build a homology model of AeDHPAAS. The plotted discrete optimized protein energy (DOPE) score profile shows regions of relatively high energy for the disordered region spanning from residues 330 to 345 (corresponding to residues 327–342 of DmDHPAAS), and the long loop at the C-terminal (Supplementary Fig. 9). PROCHECK showed that 91.4% of residues are in most favored regions, 7.5% of residues are in
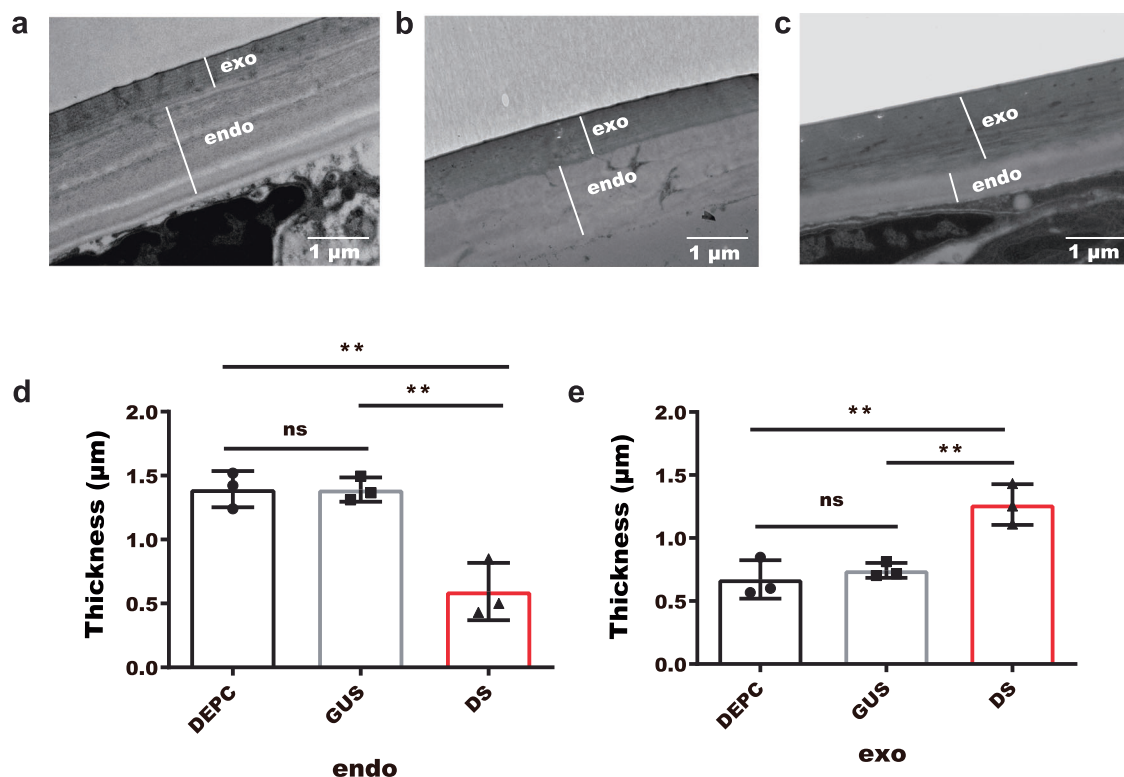
Fig. 4 | TEM analysis of adult cuticular structure after RNAi knock-down of
AeDHPAAS. **a** Natural cuticular structure after DEPC water injection. **b** Negative
control cuticular structure after *gus*-dsRNA injection. **c** Experimental cuticular
structure after *AeDHPAAS*-dsRNA injection. The scale bar in each image represents
1 μm. **d**, **e** Analysis of endocuticular layer and exocuticular layer thickness, based on
the scale of three TEM samples per group. Three mosquito cuticles were analyzed
from each group. Data were presented as mean values ± SD. An ordinary one-way
ANOVA with two-sided Tukey's multiple comparisons test was used for statistical
analysis. **d** DEPC 95% CI = 1.04–1.75; GUS 95% CI = 1.15–1.63; DS 95% CI = 0.04–1.15.

DEPC vs GUS, $Q = 0.04$, df = 6, $P = 0.97$; GUS vs DS, $Q = 8.48$, df = 6, $P < 0.01$; DEPC vs
DS, $Q = 8.51$, df = 6, $P < 0.01$. **e** DEPC 95% CI = 0.29-1.05; GUS 95% CI = 0.60-0.89; DS
95% CI = 0.86-1.67. DEPC vs GUS, $Q = 0.93$, df = 6, $P = 0.49$; GUS vs DS, $Q = 6.80$,
df = 6, $P < 0.01$; DEPC vs DS, $Q = 7.74$, df = 6, $P < 0.01$. ** indicates $P < 0.01$; ns indi-
cates no significant difference. Source data are provided as a Source Data file. exo
exocuticular layer, endo endocuticular layer, DEPC mosquitoes treated with DEPC
water, GUS mosquitoes treated with *gus*-dsRNA, DS mosquitoes treated with
AeDHPAAS-dsRNA.

additional allowed regions, and 0.4% of residues are found in outlier
regions (Supplementary Fig. 10). Verify3D indicated that 80.8% of
amino acids show an averaged 3D-1D score ≥0.2. The above statistics
indicate a reliable structure model[39–41].

To reveal possible ligand-enzyme interactions, molecular docking
experiments were carried out. AutoDock Vina docked dopa, DHPAA
and dopamine into the active site cavity (Fig. 8). The results show that
dopa is a good ligand with the highest relative binding affinity among
the 3 studied ligands (−5.6 kcal/mol) and the docking solutions of
DHPAA and dopamine resulted in binding affinities of −5.0 and
−4.9 kcal/mol, respectively. The substrate-binding pocket of AeDH-
PAAS is composed of a set of conserved residues, as well as three
variable residues (Phe82, Tyr83, and Asn195, corresponding to
DmDHPAAS Tyr79, Tyr80, and Asn192) that have diverged from the
AeDDC sequence. Phe82-Tyr83 is of particular interest as this motif is
conserved as Phe-Tyr in AeDHPAAS but is substituted to Tyr-Phe in
AeDDC. Asn195 is conserved in AeDHPAAS but is substituted for his-
tidine in AeDDC. Substitution of these three variable residues is
reported to tune bifunctional switching between DHPAAS and DDC
activities[37,42].

Considering the dimeric conformations in a physiological envi-
ronment, molecular dynamics was used to calculate the atomic
dynamic movements and conformational variations of AeDHPAAS,
DmDHPAAS, and DmDDC dimeric structures (Fig. 9, Supplementary
Table 3 and Supplementary Fig. 11). AeDHPAAS and DmDHPAAS
showed similar active site features throughout the molecular dynamics
simulations. Notably, Phe103 of DmDHPAAS and the corresponding

residue Phe106 of AeDHPAAS remained far from LLP (~4−9 Å), while
Phe103 of DmDDC remained close to LLP (~2−3 Å) throughout the
500 ns simulations (Fig. 9b).

Discussion

DHPAAS has been proposed to be involved in insect cuticle formation
since the discovery that the encoding gene confers AMD-resistance[1]. In
the current study, DHPAAS was comprehensively characterized
throughout the physiological to the molecular levels, providing a more
complete view of the role that DHPAAS plays in cuticle formation.

The physiological results revealed an abdominal phenotype after
knock-down of *AeDHPAAS* followed by injection with Ringer's solution
(Fig. 2). This could indicate a weakened abdominal cuticle due to
defects in cuticular cross-linking and a decrease in cuticle elasticity as
suggested by decreased endocuticle size[43] following *AeDHPAAS*
knockdown; however more precise measurements of insect cuticle
flexibility should be carried out in future studies. In addition, cuticle
defects were also observed in male mosquitoes (Fig. 1), and this is
consistent with our previous finding that *AeDHPAAS* is expressed at
lower levels in males[12].

The RNA-seq data of this current study shows that *AeDHPAAS*
silencing altered the expression of 117 genes encoding cuticle proteins,
106 genes involved in chitin metabolism and 109 genes involved in
lipid metabolism. Surface lipids play a fundamental role in insect
growth and development and significantly affect the structure and
physical properties of insect cuticle[44,45]. These results suggest that
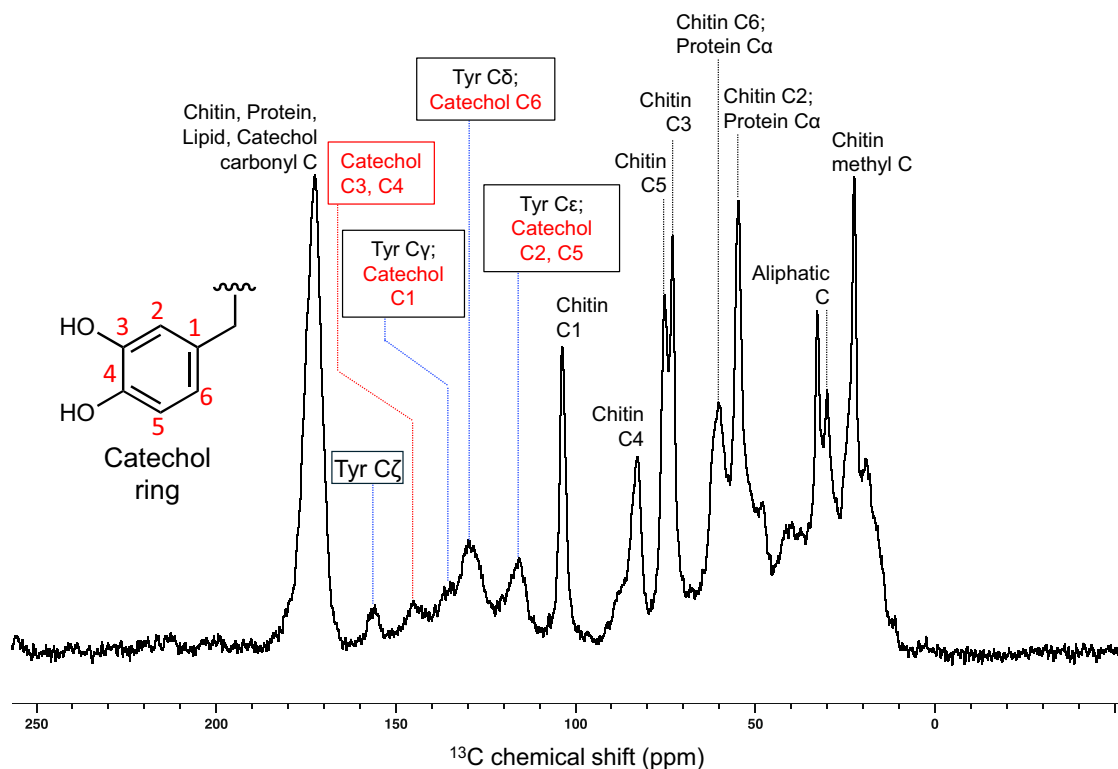*AeDHPAAS* plays direct or indirect roles in regulating the expression of

Fig. 5 | ¹³C CP/MAS NMR spectrum of *Ae. aegypti* pupal cuticles. Peaks corresponding to chitin, protein, lipid and catechol carbons are observed.

diverse genes that are responsible for producing the major cuticle components in *Ae. aegypti*.

To understand the molecular basis for DHPAAS function, the insect DHPAAS crystal structure was solved at a resolution of 2.2 Å, providing direct structural evidence to confirm that Asn192 (DmDHPAAS numbering) is indeed the key catalytic residue as previously proposed[37,42]. More importantly, an additional mechanism for oxygen delivery to the PLP cofactor can finally be proposed based on the observed hydrophobic tunnel[23,46] leading into the DmDHPAAS active center.

Comparison of the DHPAAS structure to the structure of monoamine oxidase (MAO)[47,48], which catalyzes a similar reaction, supports additional roles for active site aromatic residues. MAOs A and B contain an aromatic "sandwich" of two tyrosine residues that are believed to be involved in the oxidation of the substrate amine. The MAO-related enzyme ʟ-amino acid oxidase (LAAO) also contains a similar aromatic "sandwich" composed of two tryptophan residues[47]. This further suggests a role for the mentioned aromatic amino acid residues, Trp71, Tyr79, Tyr80, and Phe103, in the DHPAAS catalytic mechanism.

DHPAAS homologs have also been shown to convert aromatic amino acids to aryl acetaldehydes in several model plants[49,50]. While DHPAAS-like enzymes are predicted to be present in numerous other plant species, their functions remain speculative. Recently, DHPAAS from *Bombyx mori* has been applied to the biosynthesis of benzylisoquinoline alkaloids in *Escherichia coli*[42,50], raising an intriguing speculation about the possible involvement of DHPAAS or related enzymes in alkaloid pathways.

The current study provides a comprehensive view of DHPAAS function throughout the physiological level down to the molecular level, with solid-state NMR evidence for the presence of catechol-containing compounds, possibly derived from DHPAA, in the mosquito cuticle. The physiological studies further support the role of DHPAAS in cuticle formation, which is essential for

abdominal integrity, blood meal intake, and survival. These molecular views of the distinct DHPAAS crystal structure and the mosquito cuticle contribute toward a more complete understanding of PLP-dependent oxidation mechanisms and their biological relevance.

Methods
Inclusion and ethics
This research study was conducted in a manner that is consistent with the inclusion and ethics principles promoted by Nature Communications. The authors have complied with all relevant ethical regulations throughout the course of this study.

Statistical analyses
Data were presented as mean values ± standard deviation (SD). GraphPad Prism 6.02 was used to calculate SD, ordinary one-way ANOVA with two-sided Tukey's multiple comparisons test, two-way ANOVA, and the threshold level of significance as $P < 0.05$.

Abdominal injection of adult mosquitoes
Ringer's solution (150 mM NaCl, 3 mM CaCl₂, 3 mM KCl, 10 mM *N*-trimethyl-2-aminoethanesulfonic acid, and 25 mM sucrose, pH 6.9) was injected into the abdomen through the thorax of adult *Ae. aegypti* mosquitoes[24]. Male adults were injected with up to 0.4 μL of Ringer's solution; female adults were injected with up to 6 μL of Ringer's solution (Supplementary Figs. 1, 2).

RNAi knock-down of AeDHPAAS in adult mosquitoes
Purified dsRNA (2–3 μL) was injected into the thorax of adult mosquitoes 3–5 days after emergence, to knock-down transcriptional abundance according to a previous report[12]. dsRNA was injected into male and female adults. Each female adult was injected with about 2–3 μL of dsRNA. For negative and blank control groups, respectively, *E. coli β-glucuronidase* (*gus*)-dsRNA and diethylpyrocarbonate (DEPC)-treated
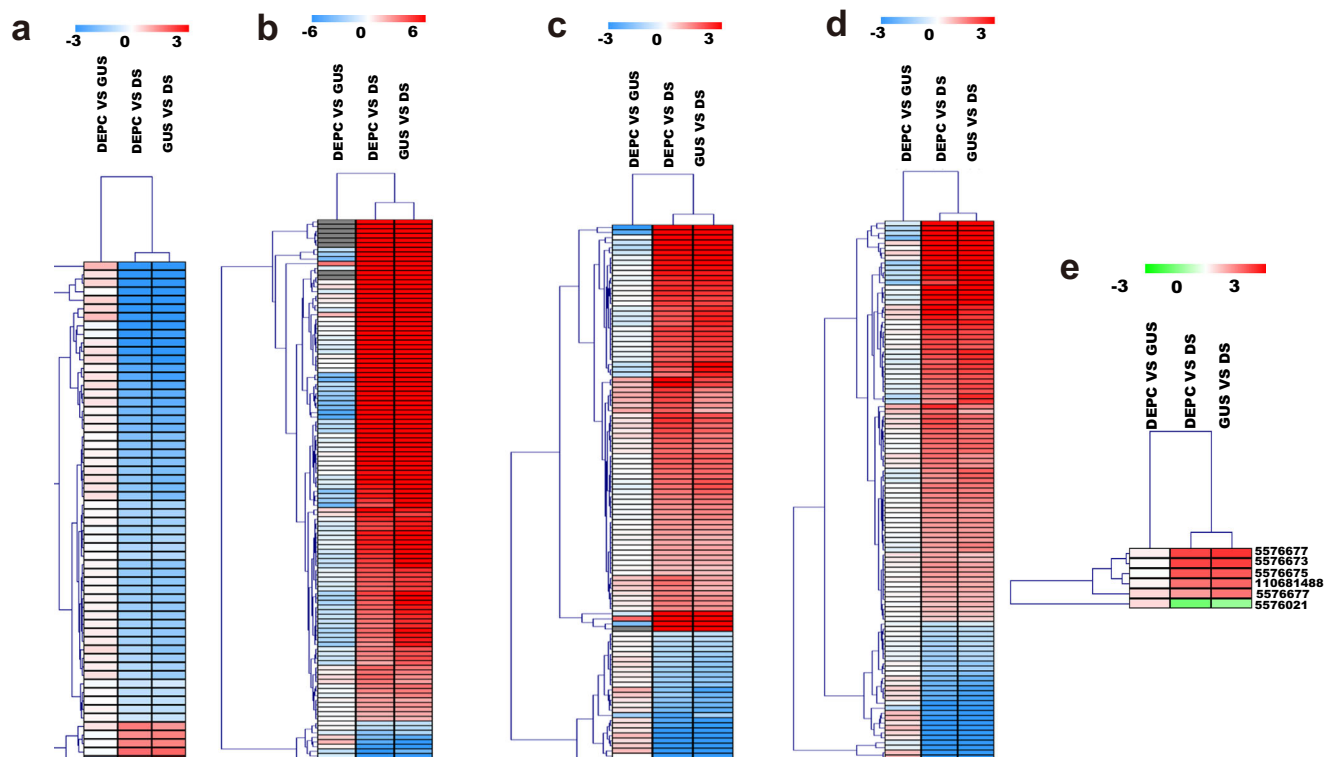
Fig. 6 | Hierarchical clustering of differentially expressed genes between control groups and the *AeDHPAAS* RNAi group. a Hierarchical clustering of differentially expressed development-related genes. **b** Hierarchical clustering of differentially expressed cuticle protein-related genes. **c** Hierarchical clustering of differentially expressed genes involved in chitin metabolism. **d** Hierarchical clustering of differentially expressed genes involved in lipid metabolism pathways.

e Hierarchical clustering of rhythmic lipid transport-related genes. Red indicates higher expression, while blue and green indicate lower expression relative to the mean value for each gene. Source data are provided as a Source Data file. DEPC treatment of adult mosquitoes with DEPC water, GUS treatment of adult mosquitoes with *gus*-dsRNA, DS treatment of adult mosquitoes with *AeDHPAAS*-dsRNA.

water were injected. Then, the relative expression of *AeDHPAAS* was detected by qPCR.

Twelve hours after RNAi injection, surviving female mosquitoes (100 mosquitoes from each treatment and control group) were selected, injected with about 4 μL of Ringer's solution, and mortalities were accounted for (Fig. 1b). In a second series of experiments, RNAi surviving female mosquitoes (50 mosquitoes from each treatment and control group) were weighed before and after blood meal, and blood meal intake weight was measured (Fig. 1c, d). Over the next 3 days after the blood meal, sugar water was given ad libitum. After oviposition occurred on the 3rd day after blood meal, the number of oviposited eggs, and their survival and hatching rate, for each mosquito, were determined (Fig. 3). Then, on the 3rd day after oviposition, the remaining surviving female adults (30 mosquitoes from each treatment and two control groups) were injected with 5 μL Ringer's solution and abdominal rupturing was accounted for. All of these experiments were replicated at least three times.

Transmission electron microscopy

Abdominal cuticles of adult mosquitoes were harvested after RNAi and before a blood meal. The harvested cuticles were fixed in 2.5 % glutaraldehyde at 4 °C overnight. The samples were washed three times for 5 min with phosphate buffer. Specimens were further fixed in 1% osmium tetroxide buffer in phosphate buffer (0.1 M, pH 7.0) at 4 °C for 1–3 h. After fixation, specimens were washed three times with phosphate buffer (0.1 M, pH 7.0) for 5 min. The samples were gradually dehydrated with 30, 50, 70, 90, 95, and 100% ethanol for 5 to 10 min at each step; the 100% ethanol step was repeated three times to ensure complete dehydration.

After dehydration, the samples were embedded in epoxy resin (Sigma-Aldrich, St. Louis, USA). The specimens were sliced with an ultramicrotome (Leica UC6; Leica, Vienna, Austria). The sections were stained with uranyl acetate (Syntechem, Changzhou, China) and lead citrate (Acros, Shanghai, China) and observed using an electron microscope (JEM1200EX; Jeol, Tokyo, Japan). TEM images were analyzed by ImageJ software.

Solid-state NMR analysis

Ae. aegypti pupal cuticles were collected into a clear paper cup after pupae emergence. The fresh cuticles were gently washed, dried, and weighed in 1.5 mL centrifuge tubes. The total weight of the dried cuticles was 65 mg.

All solid-state ^{13}C NMR measurements were performed at room temperature using two-pulse phase modulation (TPPM) decoupling, with a spinning rate of 8.5 kHz and a 4 mm ZrO$_2$ rotor. ^{13}C NMR chemical shifts were referenced to the methine carbon signal of adamantane at 28.8 ppm, relative to tetramethylsilane (TMS) at 0 ppm.

Solid-state ^{13}C cross-polarization/magic angle spinning (CP/MAS) NMR spectra of pupal cuticles and standard compounds were recorded with a fixed contact time of 2 ms. For CP/MAS experiments, the Hartmann−Hahn condition was optimized by matching radio frequency (RF) field strengths (76.9 kHz) of ^{1}H and ^{13}C. In addition, variable CP contact time-dependent ^{13}C CP/MAS spectra were acquired using contact times ranging from 0.1 to 5 ms. Measurements were performed on a Bruker DSX-400 AVANCE spectrometer equipped with a 4 mm MAS double-resonance probe (PH MAS DVT 400 WB BL4, Bruker Co, USA), and data were acquired using Bruker TopSpin 2.1 software. The spectrometer was operated at 100.4 MHz for ^{13}C
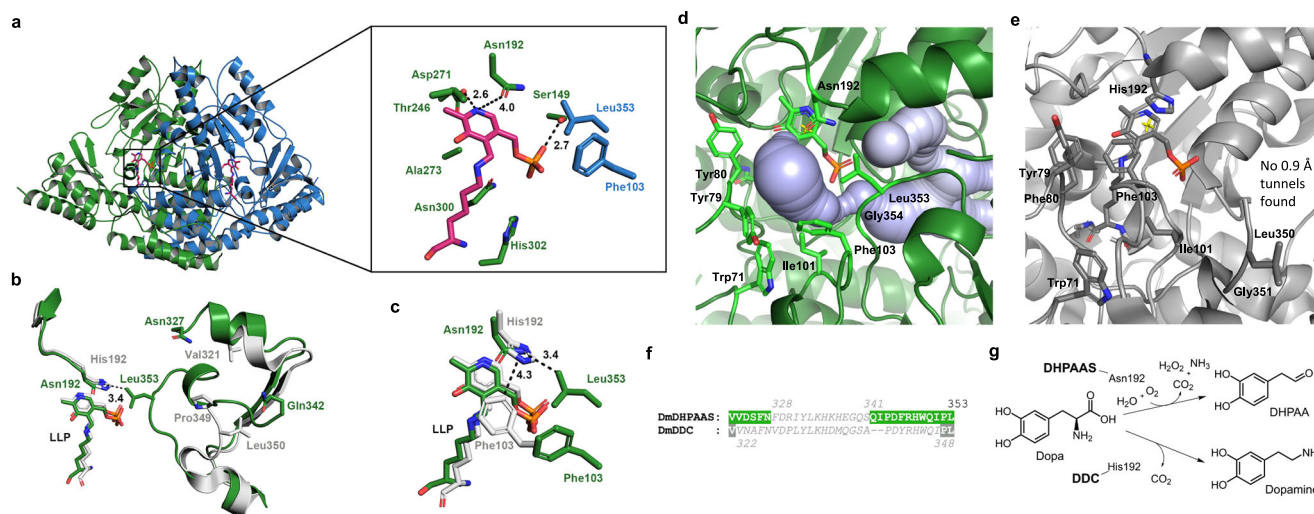
Fig. 7 | Distinct structural features of insect DHPAAS. a Overall structure (left panel) and active site (right panel) of DmDHPAAS. Lys303 forms a Schiff base with PLP, resulting in lysine-pyridoxal 5′-phosphate (LLP). LLP and key active site residues are shown in stick representation. Chain A is shown in green; the LLP from chain A is shown in magenta; chain B is shown in blue. Hydrogen bond distances and a PLP salt bridge distance are labeled. **b** Comparison of DmDHPASS and DmDDC, both in complex with PLP. DmDHPASS is shown in green, and DmDDC is shown in silver. The 320–350 region is less disordered in the DmDHPASS structure relative to that of DmDDC; accordingly, up to Asn327 can be observed in DmDHPAAS while only up to Val321 can be observed in DmDDC. **c** A closer view of the interactions with LLP is shown in stick representation. DmDHPASS Phe103 is much closer to the active center than the corresponding Phe103 of DmDDC. **d** Tunnels (blue sequential spheres) with a 1 Å minimum radius observed leading to DmDHPAAS LLP and Asn192; the yellow crosshair shows the target of the tunnel analysis. **e** No tunnels with a 0.9 Å minimum radius are observed leading to DmDDC LLP and His192; the yellow crosshair shows the target of the tunnel analysis. **f** Amino acid sequence alignment of DmDHPAAS and DmDDC disordered regions. Disordered residues are shown as gray single letter abbreviations in italics, while observed residues are shown as white single letter abbreviations surrounded by the color corresponding to their structure representations (green for DmDHPAAS and gray for DmDDC). **g** Comparison of enzymatic reactions catalyzed by DHPAAS and DDC.

nuclei,[27,51] with a decoupling power of 76 kHz, a spectral width of 60 kHz, and a recycle delay of 5 s. The ^{1}H 90° pulse length was 3.25 μs. For fixed contact-time CP/MAS spectra, 11,000 scans were collected. For variable-contact-time spectra, each spectrum included 8192 scans.

Longitudinal relaxation time measurements of ^{13}C nuclei (T_1^C) were conducted on a JEOL ECX400 spectrometer with a 400 MHz 4 mm MAS probe and Delta V5.0.6 software. The contact time was set to 2 ms, with a recycle delay of 3 s. Relaxation delay times (t) were set at 0.01, 0.05, 0.2, 0.5, 1, 2, 4.5, 10, and 15 s, for a total of nine spectra. Each spectrum included 8192 scans. The signal intensity ratio $M(t)/M(O)$ was plotted against the delay time t and fit to the exponential function shown in Eq. (1) to calculate T_1^C values.

$$\frac{M(t)}{M(0)} = A e^{\frac{-t}{T_1^C}} \tag{1}$$

Curve fitting was performed using Origin Pro 2024, using the following equation, two-component Eq. (2).

$$y = y_0 + A_1 e^{-x/t_1} + A_2 e^{-x/t_2}, \tag{2}$$

RNA-seq and analysis
To determine genes that are differentially expressed in *AeDHPAAS* knock-down mosquitoes, relative to control mosquitoes, dsRNA was fed to mosquito larvae according to our methods described in a previous report[12], and RNA-seq analysis was performed as described in a second previous report[52]. The total RNA of fourth instar larvae was extracted by tissue homogenization in TRIzol reagent (Invitrogen, Shanghai, China). cDNA was prepared and then sequenced in BGI, China. Transcript abundance was determined using RNA-seq by expectation maximization (RSEM)[53], where expression level read counts were normalized using fragments per kilobase of transcript per million mapped reads (FPKM).

Preparation of recombinant DmDHPAAS
Cloning and expression of *DmDHPAAS* from *D. melanogaster* cDNA were conducted according to previous reports[9,37]. A *DmDHPAAS* (NP_476592, isoform A) cDNA sequence was amplified from *D. melanogaster* using a forward primer with an NdeI restriction site (5′- AAAACATATGATGGATGCCAAGGAGTTTCGGG AAT-3′) and a reverse primer (5′-AAAACTCGAGTCACTGAGATT TCTCGTGCGTTG-3′) with an Xho I site. The amplified full-length NP_476592 sequence was cloned into an Impact™-CN plasmid (New England Biolabs). *E. coli* ER2566 competent cells were transformed with the recombinant plasmid and cultured at 37 °C. After induction of a 2 L culture with 0.3 mM isopropyl-1-thio-β-D-galactopyranoside, the cells were cultured at 15 °C for 24 h to produce the target protein with a fused chitin-binding domain. To inactivate serine and cysteine proteases, 1 mM phenylmethylsulfonyl fluoride was included in the lysis buffer. Recombinant protein was extracted from cells and applied to a column packed with chitin beads. Target protein, bound to the chitin beads via the fused chitin-binding domain, was subsequently cleaved by incubation under reducing conditions at 23 °C for 24 h. Cleaved protein was eluted from the column and concentrated in a Centricon YM-50 centrifuge concentrator (Millipore). The affinity purification resulted in the isolation of 80% pure DmDHPAAS. Increased protein purity was achieved after Source Q ion-exchange and gel-filtration chromatographies. Purified DmDHPAAS was concentrated to 8 mg ml^{-1} in 50 mM phosphate buffer (pH 7.5) in a Centricon YM-50 concentrator (Millipore). Protein purity was analyzed by SDS-PAGE, and protein concentration was determined with a Bio-Rad protein assay kit (Hercules, CA).

Protein crystallization and structure determination
Protein crystals were grown in 2 μL hanging drops, containing 1 μL of protein sample (8 mg/mL) and 1 μL of reservoir solution,
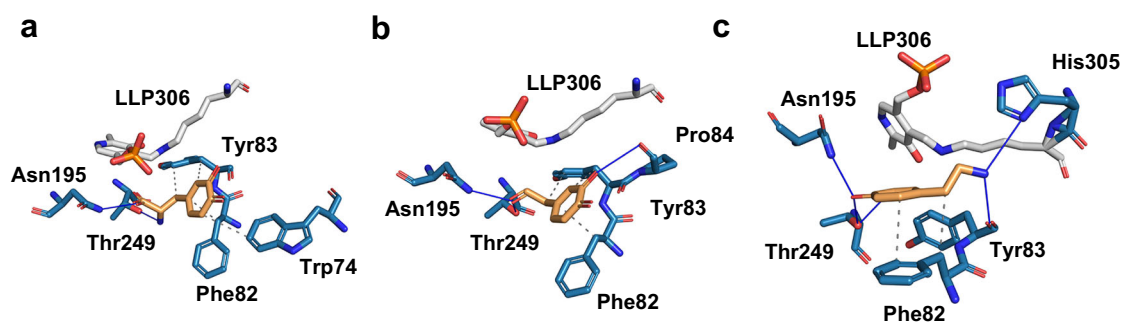
Fig. 8 | Docking of substrates and products into the AeDHPAAS active site.
DOPA (−5.6 kcal/mol) (**a**), DHPAA (−5.0 kcal/mol) (**b**), dopamine (−4.9 kcal/mol)
(**c**), active site site amino acid residues, and lysine-pyridoxal 5'-phosphate (LLP) are
shown in stick representation. Gray dashed lines indicate hydrophobic or
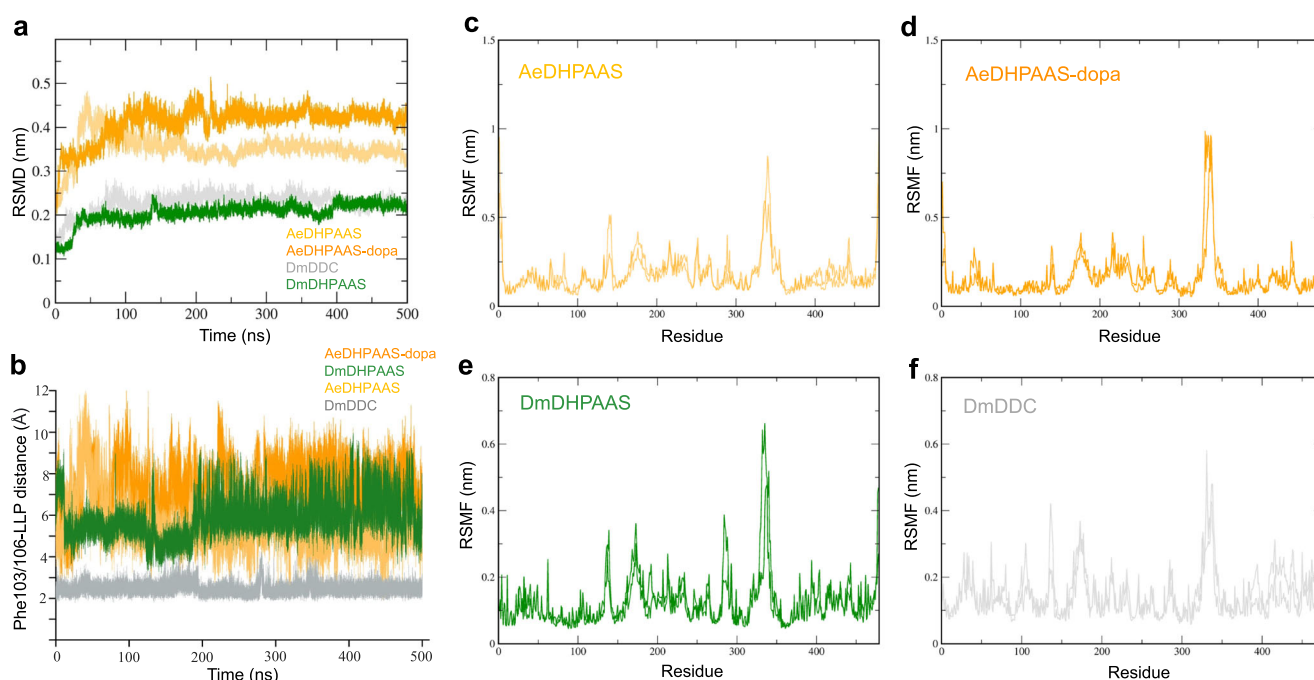carbon−carbon interactions, and blue solid lines represent hydrogen bonds.

**Fig. 9 | Comparison of molecular dynamics simulations of AeDHPAAS,
DmDHPAAS, and DmDDC over 500 ns. a** Backbone root mean square deviation
(RMSD) values for each simulation. **b** Comparison of distances between Phe103/
Phe106 and lysine-pyridoxal 5'-phosphate (LLP) in each simulation. **c**–**f** Backbone
root mean square fluctuation values for each simulation. Data from simulations of
the AeDHPAAS model with LLP, the AeDHPAAS model with LLP and dopa, the
DmDHPAAS crystal structure with LLP, and the DmDDC crystal structure with LLP
are distinguished by peach, orange, dark green, and gray lines, respectively.

suspended above reservoirs with 500 μl buffer. Optimal crystallization buffer consisted of 0.16 M MgCl$_2$, 0.085 M NaCl, pH 6.5, 25.5% w/v PEG 8000, and 15% glycerol. Individual crystals were cryogenized in crystallization buffer supplemented with glycerol to a final concentration of 20% for cryo-protection. The crystal structure of DmDHPAAS was determined using molecular replacement based on the reported structure of insect DDC (PDB ID 3K40)[22]. MOLREP[54] was used to calculate cross-rotation and translation of the model. Iterative cycles of crystallographic refinement were performed with Refmac 5.2, and model building was performed with Coot[55]. PLP cofactor was added after the R factor dropped to approximately 0.25 at full resolution, based upon 2Fo−Fc and Fo−Fc electron density. Solvent was automatically added and refined using ARP/wARP[56] and Refmac 5.2.

Analysis of protein tunnels

Tunnels in DmDHPAAS and DmDDC dimeric crystal structures were determined using CAVER 3.0.3 PyMOL Plugin[57]. Surrounding coordinates for LLP and the catalytic 192 residue (As192 or His192) in molecule A were set as the starting point, standard amino acids and LLP were selected as residues considered for tunnel calculation, minimum probe radius was set at 1 Å for DmDHPAAS and 0.9 Å for DmDDC (to demonstrate that the analysis is not biased), and other default settings were used to search for protein tunnels. The resulting tunnels were visualized in PyMOL (https://pymol.org).

Building a full-length AeDHPAAS model

The full-length sequence of AeDHPAAS (XM_001661007) was aligned with DmDHPAAS (PDB ID 6JRL) to build a homology model of

AeDHPAAS with MODELLER 10.2[58]. Models were evaluated for their quality using various structural parameters and comparative evaluation tools, such as optimized protein energy (DOPE) and molecular PDF (molpdf), PROCHECK, and the Verify3D program from the SAVES server (https://saves.mbi.ucla.edu/). Low molpdf and DOPE assessment values were considered to indicate better quality models. PROCHECK was used to check the stereochemical quality of the resulting model. Verify3D was used to determine the compatibility of an atomic model (3D) with its own amino acid sequence (1D). The best model was selected and refined with energy minimization to optimize stereochemistry using the loop model script of MODELLER 10.2. The optimized model was then used for docking and molecular dynamics simulations.

Molecular docking

AutoDock Vina[59] produced molecular docking solutions for DOPA, DHPAA, and dopamine as ligands of AeDHPAAS. Ligands and receptors were prepared with AutoDock Tools 1.5.6 (http://mgltools.scripps.edu/). The coordinates of LLP and the AeDHPAAS-LLP complex were obtained by superposing the DmDHPAAS crystal structure (PDB ID 6JRL) onto the newly built model. Partial charges for protein atoms were assigned using Kollman charges, while LLP and ligands were assigned with Gasteiger charges, making sure that presented integer charges were included for all atoms. A grid box (34 × 20 × 24 Å) with 1.0 Å spacing covered the entire active-site cavity around LLP. PLIP[60] and PyMOL were used to visualize the docking results.

Molecular dynamics

AeDHPAAS models were compared to DmDHPAAS and DmDDC structures using molecular dynamics simulations with GROMACS (version 2021). DmDHPAAS and DmDDC crystal structures are missing residues in the disordered 320–350 regions. As a result, Asn327 becomes attached to Gln342 in DmDHPAAS and Val321 becomes attached to Pro349 during structure preparation for GROMACS. Therefore, the structures of the disordered 328–341 residues of DmDHPAAS and disordered residues 322–353 of DmDDC were predicted by AlphaFold 2 using ColabFold run in ChimeraX[61,62]; then the AlphaFold-modeled disordered regions were merged with the corresponding crystal structures in Coot. Refinement of the combined structures was carried out using Coot and Refmac 5 in the CCP4 package. The AlphaFold-modeled structures, and combined structures are included as Supplementary Data 1–4. Matching molecular dynamics simulations of unmodified DmDDC and DmDHPAAS crystal structures show similar root mean square deviation (RMSD) values relative to the simulations of crystal structures with combined AlphaFold-modeled residues (Supplementary Fig. 12). Topology and parameter files for each structure were generated using the CHARMM36 force field[63], while topology and parameter files for ligands were generated by the CHARMM General Force Field (CGenFF) program[64]. TIP3P (transferable intermolecular potential 3 point) water molecules were included with neutralization by Na$^+$ ions; additional system setup information is provided in Supplementary Table 3. Dodecahedron periodic water boxes were simulated with a margin of 1.0 nm. The solvated structure was minimized by the steepest descent algorithm until the maximum force reached <1000 kJ/mol/nm at 300 K. Equilibration of the complex was performed for 100 ps at 300 K using V-rescale (modified Berendsen) thermostat with NVT ensemble (constant number of atoms, volume, and temperature). The system was then equilibrated for 100 ps at 1 atm using the Berendsen algorithm with NPT ensemble (constant number of atoms, pressure, and temperature). The LINCS algorithm constrained covalent bonds for the equilibration steps. Long-range electrostatics was calculated by using the Particle Mesh Ewald (PME) method with a Fourier grid spacing of 1.4 Å. After equilibration at 1 bar and 300 K under NPT ensemble with a time step of 2 fs, production molecular dynamics simulations were run for 200–500 ns with the time step defined as 2 fs. Trajectories were saved and XMGRACE was used to analyze results.

Reporting summary

Further information on research design is available in the Nature Portfolio Reporting Summary linked to this article.

References

1. Sourkes, T. L. Dopa decarboxylase: substrates, coenzyme, inhibitors. *Pharm. Rev.* **18**, 53–60 (1966).
2. Livingstone, M. S. & Tempel, B. L. Genetic dissection of monoamine neurotransmitter synthesis in *Drosophila*. *Nature* **303**, 67–70 (1983).
3. Osborne, R. H. Insect neurotransmission: neurotransmitters and their receptors. *Pharm. Ther.* **69**, 117–142 (1996).
4. Nappi, A. J., Carton, Y. & Vass, E. Reduced cellular immune competence of a temperature-sensitive dopa decarboxylase mutant strain of *Drosophila melanogaster* against the parasite *Leptopilina boulardi*. *Comp. Biochem. Physiol. B* **101**, 453–460 (1992).
5. Davis, M. M., Primrose, D. A. & Hodgetts, R. B. A member of the p38 mitogen-activated protein kinase family is responsible for transcriptional induction of Dopa decarboxylase in the epidermis of *Drosophila melanogaster* during the innate immune response. *Mol. Cell Biol.* **28**, 4883–4895 (2008).
6. Huang, C. Y., Chou, S. Y., Bartholomay, L. C., Christensen, B. M. & Chen, C. C. The use of gene silencing to study the role of dopa decarboxylase in mosquito melanization reactions. *Insect Mol. Biol.* **14**, 237–244 (2005).
7. Paskewitz, S. M. & Andreev, O. Silencing the genes for dopa decarboxylase or dopachrome conversion enzyme reduces melanization of foreign targets in *Anopheles gambiae*. *Comp. Biochem. Physiol. B Biochem. Mol. Biol.* **150**, 403–408 (2008).
8. Ferdig, M. T., Li, J., Severson, D. W. & Christensen, B. M. Mosquito dopa decarboxylase cDNA characterization and blood-meal-induced ovarian expression. *Insect Mol. Biol.* **5**, 119–126 (1996).
9. Vavricka, C. et al. From L-dopa to dihydroxyphenylacetaldehyde: a toxic biochemical pathway plays a vital physiological function in insects. *PLoS ONE* **6**, e16124 (2011).
10. Liao, C., Upadhyay, A., Liang, J., Han, Q. & Li, J. 3,4-Dihydroxyphenylacetaldehyde synthase and cuticle formation in insects. *Dev. Comp. Immunol.* **83**, 44–50 (2018).
11. Wang, D. & Marsh, J. L. Developmental regulation of the alpha-methyldopa hypersensitive gene of *Drosophila melanogaster*. *Dev. Biol.* **168**, 598–612 (1995).
12. Chen, J., Lu, H. R., Zhang, L., Liao, C. H. & Han, Q. RNA interference-mediated knockdown of 3, 4-dihydroxyphenylacetaldehyde synthase affects larval development and adult survival in the mosquito *Aedes aegypti*. *Parasit. Vectors* **12**, 311 (2019).
13. Black, B. C., Pentz, E. S. & Wright, T. R. The alpha methyl dopa hypersensitive gene, 1(2)amd, and two adjacent genes in *Drosophila melanogaster*: physical location and direct effects of amd on catecholamine metabolism. *Mol. Gen. Genet.* **209**, 306–312 (1987).
14. Marsh, J. L., Erfle, M. P. & Leeds, C. A. Molecular localization, developmental expression and nucleotide sequence of the alpha-

methyldopa hypersensitive gene of *Drosophila*. *Genetics* **114**, 453–467 (1986).

15. Wang, D., Marsh, J. L. & Ayala, F. J. Evolutionary changes in the expression pattern of a developmentally essential gene in three *Drosophila* species. *Proc. Natl Acad. Sci. USA* **93**, 7103–7107 (1996).

16. Tatarenkov, A., Zurovcova, M. & Ayala, F. J. Ddc and amd sequences resolve phylogenetic relationships of *Drosophila*. *Mol. Phylogenet. Evol.* **20**, 321–325 (2001).

17. Peter, M. G., Grün, L. & Förster, H. CP/MAS-¹³C-NMR spectra of sclerotized insect cuticle and of chitin†. *Angew. Chem. Int. Ed. Engl.* **23**, 638–639 (1984).

18. Schaefer, J. et al. Aromatic cross-links in insect cuticle: detection by solid-state ¹³C and ¹⁵N NMR. *Science* **235**, 1200–1204 (1987).

19. Kramer, K. J., Hopkins, T. L. & Schaefer, J. Applications of solids NMR to the analysis of insect sclerotized structures. *Insect Biochem. Mol. Biol.* **25**, 1067–1080 (1995).

20. Merritt, M. E., Christensen, A. M., Kramer, K. J., Hopkins, T. L. & Schaefer, J. Detection of intercatechol cross-links in insect cuticle by solid-state carbon-13 and nitrogen-15 NMR. *J. Am. Chem. Soc.* **118**, 11278–11282 (1996).

21. Dey, K. K. & Ghosh, M. Understanding the effect of deacetylation on chitin by measuring chemical shift anisotropy tensor and spin lattice relaxation time. *Chem. Phys. Lett.* **738**, 136782 (2020).

22. Han, Q., Ding, H., Robinson, H., Christensen, B. M. & Li, J. Crystal structure and substrate specificity of *Drosophila* 3,4-dihydroxyphenylalanine decarboxylase. *PLoS ONE* **5**, e8826 (2010).

23. Dulchavsky, M. et al. Directed evolution unlocks oxygen reactivity for a nicotine-degrading flavoenzyme. *Nat. Chem. Biol.* **19**, 1406–1414 (2023).

24. Han, Q., Hansson, B. S. & Anton, S. Interactions of mechanical stimuli and sex pheromone information in antennal lobe neurons of a male moth, *Spodoptera littoralis*. *J. Comp. Physiol. A Neuroethol. Sens. Neural Behav. Physiol.* **191**, 521–528 (2005).

25. Locke, M. Pore canals and related structures in insect cuticle. *J. Biophys. Biochem. Cytol.* **10**, 589–618 (1961).

26. Nakazawa, Y. & Asakura, T. High-resolution ¹³C CP/MAS NMR study on structure and structural transition of *Antheraea pernyi* silk fibroin containing poly(L-alanine) and Gly-rich regions. *Macromolecules* **35**, 2393–2400 (2002).

27. Nakazawa, Y., Asano, A., Nakazawa, C., Tsukatani, T. & Asakura, T. Structural characterization of silk-polyurethane composite material for biomaterials using solid-state NMR. *Polym. J.* **44**, 802–807 (2012).

28. Renneckar, S., Johnson, R. K., Zink-Sharp, A., Sun, N. & Glasser, W. G. Fiber modification by steam-explosion: 13C NMR and dynamic mechanical analysis studies of co-refined wood and polypropylene. *Compos. Interfaces* **12**, 559–580 (2005).

29. Koenig, J. L. *Spectroscopy of Polymers* 2nd edn (Elsevier Science Inc, 1999).

30. Bloembergen, N., Purcell, E. M. & Pound, R. V. Relaxation effects in nuclear magnetic resonance absorption. *Phys. Rev.* **73**, 679–712 (1948).

31. Kaji, A., Yamanaka, A. & Murano, M. Structural-analysis of polyethylene fibers by solid-state high-resolution nmr - the distribution of c-13 spin-lattice relaxation-times. *Polym. J.* **10**, 893–900 (1990).

32. Kanehisa, M. & Goto, S. KEGG: kyoto encyclopedia of genes and genomes. *Nucleic Acids Res.* **28**, 27–30 (2000).

33. Kanehisa, M. Toward understanding the origin and evolution of cellular organisms. *Protein Sci.* **28**, 1947–1951 (2019).

34. Kanehisa, M., Furumichi, M., Sato, Y., Kawashima, M. & Ishiguro-Watanabe, M. KEGG for taxonomy-based analysis of pathways and genomes. *Nucleic Acids Res* **51**, D587–D592 (2023).

35. Krissinel, E. & Henrick, K. Inference of macromolecular assemblies from crystalline state. *J. Mol. Biol.* **372**, 774–797 (2007).

36. Yano, T., Kuramitsu, S., Tanase, S., Morino, Y. & Kagamiyama, H. Role of Asp222 in the catalytic mechanism of *Escherichia coli* aspartate aminotransferase: the amino acid residue which enhances the function of the enzyme-bound coenzyme pyridoxal 5′-phosphate. *Biochemistry* **31**, 5878–5887 (1992).

37. Liang, J., Han, Q., Ding, H. & Li, J. Biochemical identification of residues that discriminate between 3,4-dihydroxyphenylalanine decarboxylase and 3,4-dihydroxyphenylacetaldehyde synthase-mediated reactions. *Insect Biochem. Mol. Biol.* **91**, 34–43 (2017).

38. Komori, H., Nitta, Y., Ueno, H. & Higuchi, Y. Structural study reveals that Ser-354 determines substrate specificity on human histidine decarboxylase. *J. Biol. Chem.* **287**, 29175–29183 (2012).

39. Sakyi, P. O. et al. Homology modeling, de novo design of ligands, and molecular docking identify potential inhibitors of *Leishmania donovani* 24-sterol methyltransferase. *Front. Cell Infect. Microbiol.* **12**, 859981 (2022).

40. Vadloori, B., Sharath, A. K., Prabhu, N. P. & Maurya, R. Homology modelling, molecular docking, and molecular dynamics simulations reveal the inhibition of *Leishmania donovani* dihydrofolate reductase-thymidylate synthase enzyme by Withaferin-A. *BMC Res. Notes* **11**, 246 (2018).

41. Sahay, A., Piprodhe, A. & Pise, M. In silico analysis and homology modeling of strictosidine synthase involved in alkaloid biosynthesis in *catharanthus roseus*. *J. Genet. Eng. Biotechnol.* **18**, 44 (2020).

42. Vavricka, C. J. et al. Mechanism-based tuning of insect 3,4-dihydroxyphenylacetaldehyde synthase for synthetic bioproduction of benzylisoquinoline alkaloids. *Nat. Commun.* **10**, 2015 (2019).

43. Dirks, J. H. & Durr, V. Biomechanics of the stick insect antenna: damping properties and structural correlates of the cuticle. *J. Mech. Behav. Biomed. Mater.* **4**, 2031–2042 (2011).

44. Hendricks, G. M. & Hadley, N. F. Structure of the cuticle of the common house cricket with reference to the location of lipids. *Tissue Cell* **15**, 761–779 (1983).

45. Wang, Y., Yu, Z., Zhang, J. & Moussian, B. Regionalization of surface lipids in insects. *Proc. Biol. Sci.* **283**, 20152994 (2016).

46. Hiraka, K. et al. Structure of lactate oxidase from *Enterococcus hirae* revealed new aspects of active site loop function: product-inhibition mechanism and oxygen gatekeeper. *Protein Sci.* **31**, e4434 (2022).

47. Gaweska, H. & Fitzpatrick, P. F. Structures and mechanism of the monoamine oxidase family. *Biomol. Concepts* **2**, 365–377 (2011).

48. Binda, C., Newton-Vinson, P., Hubalek, F., Edmondson, D. E. & Mattevi, A. Structure of human monoamine oxidase B, a drug target for the treatment of neurological disorders. *Nat. Struct. Biol.* **9**, 22–26 (2002).

49. Liang, J., Han, Q., Tan, Y., Ding, H. & Li, J. Current advances on structure-function relationships of pyridoxal 5′-phosphate-dependent enzymes. *Front. Mol. Biosci.* **6**, 4 (2019).

50. Vavricka, C. J. et al. Machine learning discovery of missing links that mediate alternative branches to plant alkaloids. *Nat. Commun.* **13**, 1405 (2022).

51. Bennett, A. E., Rienstra, C. M., Auger, M., Lakshmi, K. V. & Griffin, R. G. Heteronuclear decoupling in rotating solids. *J. Chem. Phys.* **103**, 6951–6958 (1995).

52. Zhang, L. et al. Arylalkalamine N-acetyltransferase-1 functions on cuticle pigmentation in the yellow fever mosquito, *Aedes aegypti*. *Insect Sci.* **28**, 1591–1600 (2021).

53. Li, B. & Dewey, C. N. RSEM: accurate transcript quantification from RNA-Seq data with or without a reference genome. *BMC Bioinformatics* **12**, 323 (2011).

54. Vagin, A. & Teplyakov, A. MOLREP: an automated program for molecular replacement. *J. Appl. Crystallogr.* **30**, 1022–1025 (1997).

55. Emsley, P., Lohkamp, B., Scott, W. G. & Cowtan, K. Features and development of Coot. *Acta Crystallogr. D. Biol. Crystallogr.* **66**, 486–501 (2010).

56. Langer, G., Cohen, S. X., Lamzin, V. S. & Perrakis, A. Automated macromolecular model building for X-ray crystallography using ARP/wARP version 7. *Nat. Protoc.* **3**, 1171–1179 (2008).
57. Pavelka, A. et al. CAVER: algorithms for analyzing dynamics of tunnels in macromolecules. *IEEE/ACM Trans. Comput. Biol. Bioinforma.* **13**, 505–517 (2016).
58. Webb, B. & Sali, A. Comparative protein structure modeling using MODELLER. *Curr. Protoc. Protein Sci.* **86**, 37 (2016).
59. Trott, O. & Olson, A. J. AutoDock Vina: improving the speed and accuracy of docking with a new scoring function, efficient optimization, and multithreading. *J. Comput. Chem.* **31**, 455–461 (2010).
60. Adasme, M. F. et al. PLIP 2021: expanding the scope of the protein-ligand interaction profiler to DNA and RNA. *Nucleic Acids Res.* **49**, W530–W534 (2021).
61. Mirdita, M. et al. ColabFold: making protein folding accessible to all. *Nat. Methods* **19**, 679–682 (2022).
62. Meng, E. C. et al. UCSF ChimeraX: tools for structure building and analysis. *Protein Sci.* **32**, e4792 (2023).
63. Huang, J. et al. CHARMM36m: an improved force field for folded and intrinsically disordered proteins. *Nat. Methods* **14**, 71–73 (2017).
64. Vanommeslaeghe, K. et al. CHARMM general force field: a force field for drug-like molecules compatible with the CHARMM all-atom additive biological force fields. *J. Comput. Chem.* **31**, 671–690 (2010).

Acknowledgements

Author contributions

J.C. (Jing Chen), C.J.V., S.W., Y.N., Y.M., H.C., Y.T., J.L. (Jing Liang), J.K.C. (Jiukai Chen), Y.H., K.N., T.H., H.G., J.Y.L. (Jianyong Li), C.L., and Q.H. performed experiments and analyzed data; Q.H., C.L., Y.N., and C.J.V. conceived the experiments; C.J.V., J.C., S.W., C.L. and Q.H. wrote the manuscript. All authors read the manuscript.

Competing interests

The authors declare no competing interests.

Additional information

Supplementary information The online version contains supplementary material available at https://doi.org/10.1038/s41467-025-59723-0.

Correspondence and requests for materials should be addressed to Christopher J. Vavricka, Chenghong Liao or Qian Han.

Peer review information *Nature Communications* thanks Elena Andreeva, Tian Liu, Pushpa Rampratap and the other, anonymous, reviewer(s) for their contribution to the peer review of this work. A peer review file is available.

Reprints and permissions information is available at http://www.nature.com/reprints

Publisher's note Springer Nature remains neutral with regard to jurisdictional claims in published maps and institutional affiliations.

[1]Laboratory of Tropical Veterinary Medicine and Vector Biology, School of Life and Health Sciences, Hainan Province Key Laboratory of One Health, Collaborative Innovation Center of Life and Health, Hainan University, Haikou, Hainan 570228, China. [2]Hainan International One Health Institute, Hainan University, Haikou, Hainan 570228, China. [3]Department of Biotechnology and Life Science, Graduate School of Engineering, Tokyo University of Agriculture and Technology, Koganei, Tokyo 184-8588, Japan. [4]Hainan Vocational University of Science and Technology, Haikou, Hainan 571126, China. [5]Department of Biochemistry, Virginia Polytechnic Institute and State University, Blacksburg, Virginia 24061, USA. [6]Engineering Biology Research Center, Kobe University, Kobe 657-8501, Japan. [7]These authors contributed equally: Jing Chen, Christopher J. Vavricka, Shuangshuang Wei. ✉e-mail: chris@go.tuat.ac.jp; liaochh@hainanu.edu.cn; qianhan@hainan.edu.cn